Original Article

Computational Fontan Analysis: Preserving Accuracy While Expediting Workflow

Xiaolong Liu, PhD[1,2,*], Seda Aslan, MSc[1,2,*], Byeol Kim, MSc[1,2],
Linnea Warburton, BSc[2], Derrick Jackson, BSc[2], Abir Muhuri, BSc[2],
Akshay Subramanian, MSc[2], Paige Mass, BSc[3], Vincent Cleveland, MS[3],
Yue-Hin Loke, MD[4], Narutoshi Hibino, MD, PhD[5], Laura Olivieri, MD[3,4],
and Axel Krieger, PhD[1,2]

Abstract

Background: Postoperative outcomes of the Fontan operation have been linked to geometry of the cavopulmonary pathway, including graft shape after implantation. Computational fluid dynamics (CFD) simulations are used to explore different surgical options. The objective of this study is to perform a systematic *in vitro* validation for investigating the accuracy and efficiency of CFD simulation to predict Fontan hemodynamics. **Methods:** CFD simulations were performed to measure indexed power loss (iPL) and hepatic flow distribution (HFD) in 10 patient-specific Fontan models, with varying mesh and numerical solvers. The results were compared with a novel *in vitro* flow loop setup with 3D printed Fontan models. A high-resolution differential pressure sensor was used to measure the pressure drop for validating iPL predictions. Microparticles with particle filtering system were used to measure HFD. The computational time was measured for a representative Fontan model with different mesh sizes and numerical solvers. **Results:** When compared to *in vitro* setup, variations in CFD mesh sizes had significant effect on HFD ($P = .0002$) but no significant impact on iPL ($P = .069$). Numerical solvers had no significant impact in both iPL ($P = .50$) and HFD ($P = .55$). A transient solver with 0.5 mm mesh size requires computational time 100 times more than a steady solver with 2.5 mm mesh size to generate similar results. **Conclusions:** The predictive value of CFD for Fontan planning can be validated against an *in vitro* flow loop. The prediction accuracy can be affected by the mesh size, model shape complexity, and flow competition.

Introduction

Fontan surgery is performed as the final step in surgical palliation of single ventricle heart disease. By surgically connecting the inferior vena cava (IVC) to the pulmonary arteries (PA) and bypassing the heart, the pulmonary and systemic circulations are separated, generally allowing for more efficient oxygen delivery for the patient. The shape and implantation of Fontan grafts and the resultant geometry of the Fontan cavopulmonary pathway affects long-term outcomes,[1–3] including pulmonary arteriovenous malformations (PAVM),[2] decreased exercise capacity, underdeveloped PA, and thrombosis. These complications are linked to hemodynamics in postoperative Fontan geometries.[3] The correlation between the development of PAVM and hepatic flow distribution (HFD)[4–6] and the negative correlation between decreased exercise capacity and power loss in Fontan[7] have been demonstrated by various groups.

Predicting the best shape and implantation of the Fontan graft involves balancing several different, sometimes opposing goals, including but not limited to balancing HFD and reducing power loss.[8,9] Computational fluid dynamics (CFD) simulation

has been employed to explore different surgical options and to assist in predicting postoperative hemodynamic performance.[10,11] Previously, the reliability of CFD simulations has been linked mainly to the solver assumptions and boundary conditions (BC).[12] Implantation of the Fontan grafts as

[1] Department of Mechanical Engineering, Johns Hopkins University, Baltimore, MD, USA
[2] Department of Mechanical Engineering, University of Maryland, College Park, MD, USA
[3] Sheikh Zayed Institute for Pediatric Surgical Innovation, Children's National Medical Center, Washington, DC, USA
[4] Division of Cardiology, Children's National Medical Center, Washington, DC, USA
[5] Department of Cardiac Surgery, University of Chicago/Advocate Children's Hospital, Chicago, IL, USA

*These authors contributed equally to this article.

Corresponding Author:
Axel Krieger, Department of Mechanical Engineering, Johns Hopkins University, 116 Hackerman Hall, 3400 N. Charles Street, Baltimore, MD 21218, USA.
Email: axel@jhu.edu

Abbreviations:

3D	three-dimensional
BC	boundary conditions
CAD	computer-aided design
CFD	computational fluid dynamics
HFD	hepatic flow distribution
iPL	indexed power loss
IVC	inferior vena cava
MRA	magnetic resonance angiography
LPA	left pulmonary artery
PA	pulmonary arteries
PAVM	pulmonary arteriovenous malformations
PL	power loss
RPA	right pulmonary artery
SCPC	superior cavopulmonary connection
SVC	superior vena cava
SIMPLE	semi implicit method for pressure linked equations

prescribed by the preoperative surgical plan relies on the surgeon's experience.[13] In addition, even if perfect Fontan graft implantation can be achieved, the geometry of the vessel will be deformed due to the growth of the patient.

Realistic use of preoperative Fontan planning requires development of a tool that is quick, easy to use, requires standard clinical data for its inputs, and can turnaround accurate recommendations quickly and clearly to ensure implantation of Fontan designs with good performance. Automatic optimization of Fontan pathway geometry involves computing

Figure 1. The cohort of 3D reconstructed Fontan models. EX and LT represent extracardiac and lateral tunnel, respectively. All the models were preprocessed by making clean cuts at IVC, SVC, LPA, and RPA for defining the areas of inlet/outlet BC. The cohort represents a variety of model geometry, different numbers of inlets, and different anatomy conditions, such as the existence of coartation in EX2 and EX5.
Abbreviations: SVC, superior vena cava; IVC, inferior vena cava; LPA, left pulmonary artery; RPA, right pulmonary artery.

thousands of Fontan hemodynamics simulation to identify the optimal surgical option for each patient.[10] Fast Fontan computation with reasonable accuracy is essential to facilitate these developments allowing for more efficient iterative designs, and creation of multiple similar designs to account for small variations in surgical implantation. Prior research demonstrated discrepancies between the preoperative and postoperative results,[6] however, it is difficult to separately quantify the relative contribution of errors in CFD prediction, surgical implantation, and vessel structure alternation to the difference between predicted and observed hemodynamics. Additionally, there is a "law of diminishing returns" when using additional and more powerful computational resources which require time and expense for surgical planning. Therefore, it is crucial to explicitly analyze each error source for improving the surgical planning accuracy.

The reliability of CFD simulations is the foundational step towards accurate Fontan surgical planning. As the accuracy of CFD simulations is a primary concern in the U.S. Food and Drug Administration (FDA) regulatory practice, experimental validations of CFD have been conducted in many research studies to characterize the flow field. Computational imaging techniques and/or optical imaging methods[14] are used to visualize *in vivo* and *in vitro* flow field. 4D flow MRI data have been applied to validate hemodynamic parameters computed from CFD simulation such as flow velocities,[15] HFDs,[16–18] wall shear stress,[19] viscous dissipation.[20]

The objective of this study was to investigate the accuracy and efficiency of CFD simulation to predict Fontan hemodynamics using an *in vitro* mock circulatory benchtop setup. The impact of mesh size and numerical solver on model accuracy was evaluated to understand overall computational efficiency. In addition, this study provided a template to validate CFD simulation with similar considerations in other cardiovascular surgical planning applications beyond Fontan surgery.

Methods

Data Acquisition, Image Segmentation, and 3D Model Reconstruction

This work is approved under Children's National Institutional Review Board (IRB) Protocol Pro00013357. The patient's consent was waived due to the retrospective review of data. Anonymized data from MRIs of 10 patients with Fontan circulation were used to create 3D anatomic replicas of the Fontan and proximal thoracic vasculature. Specifically, angiography data with late-phase, nongated, and breath-held acquisition with resolution 1.4×1.4 mm were used to segment and create the 3D replica using medical image segmentation software, Mimics (Materialise) and our lab's standard approach[8] (Supplemental material Figure S1). Phase contrast images with resolution 1.5 to 2.2 mm, velocity encoding ranging 100 to 150 cm/s, and 30 reconstructed phases were used to extract flow curves for inlet and outlet BC specific to the patient. Attributes of the 10 patient-specific models are illustrated in
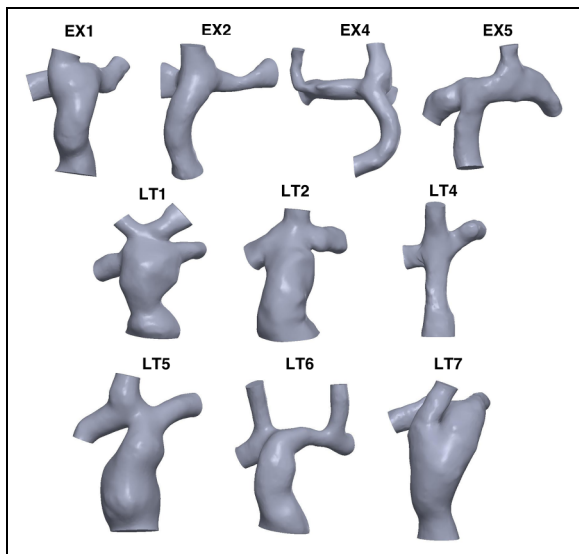
Figure 1. The BC obtained from the patient's *in vivo* 4D flow MRI data were directly used in the Fontan CFD analysis.

Hemodynamic Parameters of Interest

Fontan Efficiency: Indexed Power Loss (iPL). iPL is a numerical representation of the power loss inside the Fontan conduit regarding each patient's physiological conditions. The high iPL represents increased pressure changes in blood flow, which can exacerbate the cardiac performance.[7] The iPL equation is as follows:

$$iPL = \frac{PL}{\rho Q_s^3 / BSA^2}$$

where ρ is the density, Q_s is the systemic venous flow, and BSA is the body surface area of the patient. The power loss PL is calculated by:

$$PL = \sum_{inlets} \int_A \left(p + \frac{1}{2}\rho v^2 \right) v \times dA - \sum_{outlets} \int_A \left(p + \frac{1}{2}\rho v^2 \right) v \times dA$$

where A is the boundary area, p is the static pressure, and v is the velocity.

Hepatic Flow Distribution. The HFD is the ratio of blood flowing to the PA from the IVC. The HFD was estimated through the Lagrangian particle tracking approach to track the blood flow streamlines in CFD. By releasing massless particles on the IVC boundary surface, the particles are traced to identify the number of particles that arrived at each ending of the PA (N_{RPA} and N_{LPA}, respectively). HFD can thus be defined by the following equations:

$$HFD_{LPA} = \frac{N_{LPA}}{N_{tot}}$$

$$HFD_{RPA} = \frac{N_{RPA}}{N_{tot}}$$

where N_{tot} represents the total number of particles that are released from the IVC.

Boundary Conditions

Due to the passive venous flow from the cavae into the PA, prior studies have demonstrated accuracy of modeling continuous flow in the venous system.[21] Previous simulation studies showed good agreement between using time-averaged and pulsatile BC in simulating Fontan hemodynamics.[22] Therefore, in this study, the IVC and superior vena cava (SVC) flow rates were time averaged through summing up the phase velocity data, then divided by the overall time phase for inlet flow BC. The flow rates of the PA were assigned as the ratio of the flow split to the LPA and to RPA. The patient-specific data and the BC of the Fontan models are summarized in Table 1.

In Vitro Validation Experimental Platform

3D-Printing of Fontan Models. The *in vitro* study requires 3D-printing of Fontan models to be tested in the flow loop system that simulates the blood circulation in the total cavopulmonary connections. To connect the physical Fontan models to 15.875 mm (5/8″) tubing, a 30 mm extension was made on each inlet and outlet for fluid flow stabilization (Supplemental material Figure S2). To connect the eventual physical model to the tubing, a 20 mm long cylinder of the same diameter was added, separated from the previous extension by a loft of a determined length to create a 7° wall angle to minimize the separation of the flow.[23] A 3.175 mm (1/8″) shell was created around the model with open ends. This thickness is selected to match the thickness of the tubing the model would be connected to. The 3D models were printed by a third-party company (Xometry) using selective laser sintering (SLS) in Nylon 12 material.

Flow Loop Setup

In vitro validation of the simulation results was performed by setting up a flow loop to mimic the circulation of the 3D-printed Fontan models. Figure 2 shows the diagram of the system setup. 3D-printed Fontan models were connected to the experimental flow loop that consists of a flow pump (Flojet 04300143A Electric Pump, Xylem Inc), a fluid reservoir, Tygon tubing (OD 7/8″, ID 5/8″, McMaster-Carr), a customized compliance chamber, 4 inline ultrasonic flow meters (F-4600 Inline Flow Meter, ONICON Inc), and gate valves (2621-005G, PVC Valve, Spears Manufacturing Company). 60/40 water–glycerol mixtures were used to match the flow properties of blood.[24–26]

Measurement of iPL

We employed a differential pressure sensor (Omega Engineering Inc) with a resolution of 0.03 mmHg to measure the differential pressures (Supplemental material Figure S3). The PL can thus be calculated by using the measurements (Formula S1). To obtain robust and accurate measurements, we eliminate the effect of hydrostatic pressure (Δp_0) from different poses of Fontan models by subtracting Δp_0 from the measured Δp (Supplemental material Figure S4).

Measurement of HFD

Micro-polyethylene particles with diameters of 850–1000 μm (Cospheric LLC) were employed to suspend in water–glycerol mixture and inject to the tubing connected to IVC by using a syringe. The injected particles moved along with the fluid flow, exited from LPA and RPA, and were captured separately by a customized particle filtering tank (Supplemental material Figure S3). To make the microparticles well distributed in the fluid, we apply polysorbate as surfactant on the surface of the particles. The flow rate of particle injection from the syringe

Table 1. Patient Demographics (n = 10).

Case ID	Fontan type	Cardiac anatomy	BSA (m^2)	SVC (mL/s)	IVC (mL/s)	LPA (mL/s)	RPA (mL/s)
EX1	Extracardiac	Hypoplastic left heart syndrome	1.457	21.69	43.21	23.57	41.33
EX2	Extracardiac	Hypoplastic left heart syndrome	1.593	23.05	40.29	27.55	35.78
EX4	Extracardiac	Dextrocardia-unbalanced atrioventricular canal-bilateral glenn	1.472	L: 10.01, R: 17.22	58.91	42.21	41.9
EX5	Extracardiac	Dextrocardia- unbalanced atrioventricular canal—lglenn	1.755	26.17	46.17	51.34	21
LT1	Lateral tunnel	Levo-transposition of the great arteries—remote ventricular septal defect	1.984	L: 5.62, R: 5.62	58.77	42.34	27.68
LT2	Lateral tunnel	Double-inlet left ventricle—pulmonary atresia	1.535	15.49	60.02	34.1	41.4
LT4	Lateral tunnel	Tricuspid atresia	1.645	23.46	48.1	42.87	28.69
LT5	Lateral tunnel	Tricuspid atresia—dextro-transposition of the great arteries—ventra septal defect	1.625	16.21	32.91	23.68	25.45
LT6	Lateral tunnel	Tricuspid atresia—bilateral SVC	2.255	L: 11.15, R: 10.84	71.2	60.45	32.83
LT7	Lateral tunnel	Double-inlet left ventricle	1.767	23.08	64	49.39	37.69

Abbreviations: BSA, body surface area; SVC, superior vena cava; IVC, inferior vena cava; LPA, left pulmonary artery; RPA, right pulmonary artery.
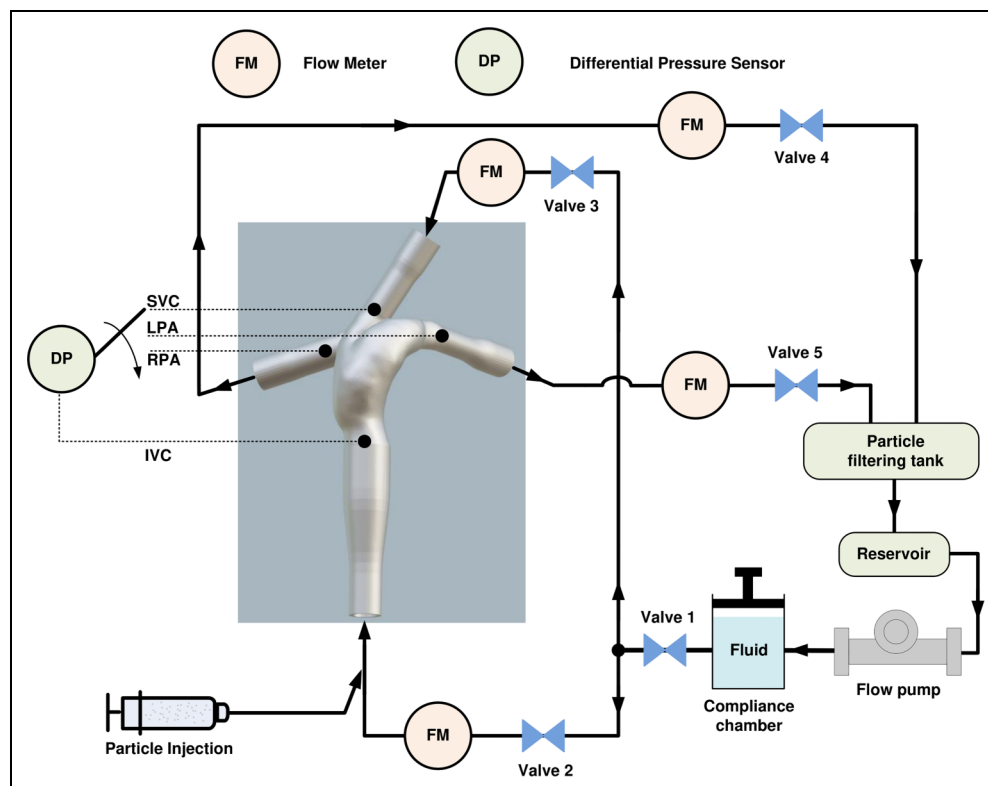

Figure 2. *In vitro* experimental setup. The experiment setup shows a 3D-printed Fontan model with 2 inlets and 2 outlets to connect with the flow loop. The fluid flow was generated by a flow pump with adjustable flow rates. Gate valves and flow meters (FMs) were used to adjust the flow rates that were prescribed at the inlets and outlets of the selected Fontan model. Microparticles were injected at the IVC and sorted by the particle filtering tank for measuring the hepatic flow distribution. A differential pressure sensor (DP) was used to measure the pressure differences of IVC-SVC, IVC-LPA, and IVC-RPA for calculating the iPL.
Abbreviations: SVC, superior vena cava; IVC, inferior vena cava; LPA, left pulmonary artery; RPA, right pulmonary artery.

was controlled below 1 mm-s^{-1} to minimize the flow interruption at IVC. A customized particle dryer was used to dehydrate microparticles. An analytical scale with 0.001 g resolution was used to weigh the microparticles in different containers. The HFD is estimated by the weight ratio (Supplemental material Figure S5).

CFD Simulation

The workflow of the CFD simulation method is shown in Figure 3. The computational models were created by including extensions at the inlet and outlet boundaries of the models. The length of the extension at the inlet was chosen to be 10 times the inlet diameter as it produced insignificant differences in hemodynamics when compared with the results that were obtained by using real velocity profiles.[27] The outlet boundaries were extended 50 mm to avoid backflow.[9] The inlet extensions will significantly increase the computation time. To address the problem, the velocity field of each model using 1 mm mesh size with 10 times inlet extension was precomputed. We extracted the velocity profiles 10 mm away from the actual SVC and IVC inlets (Supplemental material Figure S6).

The total volume of each model was divided into small tetrahedral volumes with different mesh sizes 1.5, 1, 0.7, and 0.5 mm by using Ansys mesh. Seven-layer inflation with smooth growth was applied to the model walls, excluding extensions to better capture the velocity gradients.

Three types of solvers, including SIMPLE steady-state, coupled steady-state, and SIMPLE transient, were investigated by applying 0.5, 0.7, and 1 mm mesh sizes to all models. Both the steady and transient flow equations formulated as follows were solved using time-averaged flow rates at the SVC and IVC inlets, and the percentages of total inflow at the LPA and RPA outlets.[8] The BC of the Fontan models are presented in Table 1.

Statistics

For all simulations and experiments, data are represented graphically as scatter plots of individual values with a bar identifying the median. Mean and standard deviation of each data group are represented as mean ± standard deviation. Comparisons of CFD and experiment results were analyzed using the paired 2-tailed *t*-test. A *P* value <.05 was considered statistically significant. Statistical analysis was performed by using Prism version 9 (GraphPad Software).

Results

Comparison of CFD and In Vitro Results

Because of the significant impact of different mesh sizes and the insignificant impact of different solvers on the CFD results (Supplemental material Figure S7 and Figure S8), we compared the CFD results with the experimental results by using 0.7 and 1 mm by using the SIMPLE-steady solver, as shown in Figures

4A and B. The green, blue, and red bars indicate the CFD results using (1) 0.7 mm, (2) 1 mm mesh sizes, and (3) the experiment results for iPL and HFD, respectively.

Figures 4C and D show the percentage difference of iPL, HFD with 2 comparison groups: (1) 0.7 mm mesh CFD simulation versus experimental results (0.7 vs Exp), and (2) 1 mm mesh CFD simulation versus experimental results (1 vs Exp). Figure 4C shows the medians of the percentage difference of iPL between CFD and experiment are smaller than 10% for "0.7 versus Exp" (15.57% ± 20.83%) and "1 versus Exp" (15.82% ± 19.12%). The 2 groups have no significant difference *P* = .9775. In contrast, Figure 4D shows the HFD simulation results with 1 mm mesh size have a significantly smaller difference with the experimental results than those of 0.7 mm mesh size (*P* = .0087). The medians, means, and standard deviations are 17.39%, 18.93% ± 10.63% for "0.7 versus Exp"; and 3.47%, 6.95% ± 7.25% for "1 versus Exp".

Computation Efficiency

The computation time depends on the computing power, number of iterations, mesh sizes, and numerical solver types. As the mesh size decreases, the number of mesh elements increases. Using different solvers (steady SIMPLE, steady coupled, transient SIMPLE) and various mesh sizes (0.5–2.5 mm) for the simulations, the required computation time for 3000 iterations (24 CPU cores for each simulation) was shown in Figure 5 for one of the models (EX5). This is a representation of how the time that requires to complete the simulations varies by using different solvers and mesh sizes. The steady-SIMPLE solver with the 2.5 mm mesh size shows the highest computation efficiency (9.2 min) for providing over 90% iPL and HFD prediction accuracy. While the transient solver with 0.5 mm mesh size shows the lowest computation efficiency (937 min). Despite of the fast computation speed by using 2.5 mm mesh size, we tend to keep the mesh size below 1 mm for preventing potential simulation failures with the excessively large meshes.

Discrepancy Analysis for iPL

Large discrepancy of iPL between the experimental and CFD results was seen in models: LT2, LT4, and EX5. To investigate the sources of this discrepancy, the anatomy of the models and flow fields were compared. First, the offset between the IVC and SVC centerline and the angle between the SVC and IVC flow entering the PA were presented in Figure 6. The Fontan model LT4 was used to show where the angle and offset were measured. The flow streamlines for the models were shown in each model. The flow competition between IVC and SVC flows is evident, especially for the models with smaller offsets and larger angle. The models, which have higher discrepancy in iPL (EX5, LT2, and LT4), have the IVC and SVC flows entering the PA with almost 90° (γ and β, respectively). The vortices are formed and the flow in the PA becomes more complex and difficult to model when
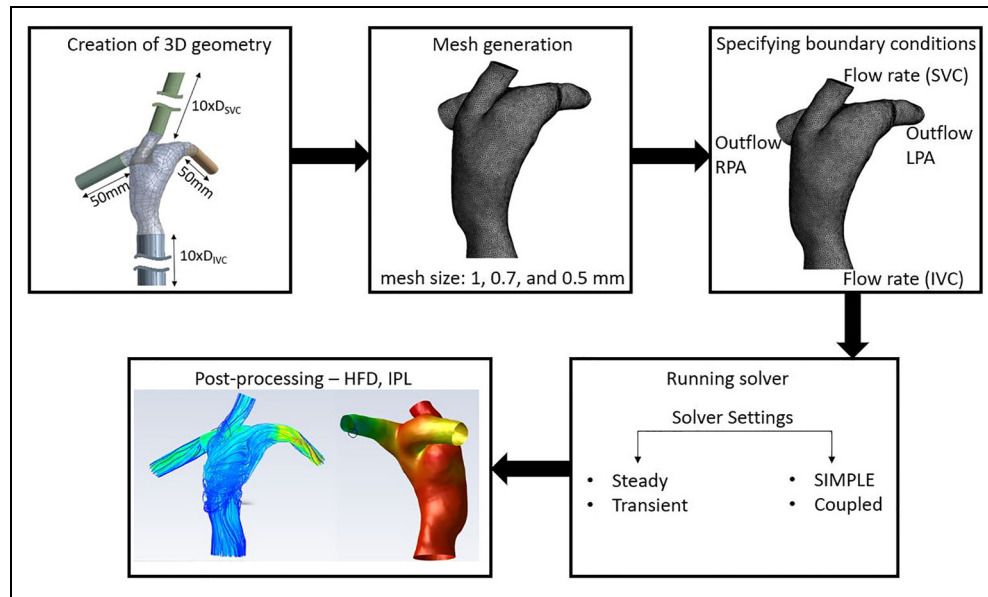
Figure 3. Procedure of computational fluid dynamics (CFD) simulation.

the inflows hit the PA wall or each other at 90°. Furthermore, the region where the SVC and IVC flows hit each other is where most of the power is dissipated. For example, 78% and 64% of the total power in LT2 and LT4 is dissipated in this region, respectively.

Discussion

Fontan surgical planning by using CFD analysis has gained a great attention from clinicians to provide valuable insight into possible postsurgical outcomes and reduce uncertainty in decision making and personalizing surgical approaches for each patient. However, CFD research has not yet translated into broad clinical acceptance because most surgical planning processes are primarily operated by engineering teams, and the surgical planning has thus been relegated to retrospective posthoc analysis. In clinical application, the required time between preoperative imaging that is used for CFD analysis and Fontan surgery can vary, but on average takes around 2 months.[3,28] Considering that at least 1000 Fontan operations occur nationally per year,[29] very limited number of clinicians can be supported by qualified engineering teams for performing Fontan surgical planning tasks. There is a need to develop a software tool for clinicians in order to reduce the need of engineering teams. The computation efficiency of Fontan simulation is one of the key issues to realize this goal. In this study, we found that there are diminishing returns on investment for both mesh size and solver sophistication of CFD simulation; and can recommend standards to provide clinically acceptable Fontan predictions, allowing for realistic clinical use. We also identified that there are certain Fontan geometries that may be prone to more discrepancies and would warrant clinicians to be cautious of the CFD results of these types of Fontan geometries.

This study aimed to quantify both the accuracy and efficiency of different CFD setups for Fontan surgical planning, validated by a sophisticated *in vitro* bench setup. A key innovation of this work was development of an *in-vitro* micro particle tracking system for reliable HFD *in vitro* measurements. Prior research studies employ 4D flow MRI data and particle tracking method to estimate HFD.[16–18] However, the 4D flow MRI itself may require validation by using PIV[20] or CFD simulation[21] due to its limited spatial resolution, signal noise, and the segmentation errors. To the best of our knowledge, this is the first use of an *in vitro* flow loop setup to validate HFD with a large enough cohort size for a statistical comparison.

The clinical impact of iPL is with regards to the patient's exercise capacity that is known to deteriorate over time,[30] while the HFD, which is diversion of normal hepatic venous flow from the pulmonary circulation, is related to the development of PAVM.[31] In our CFD mesh analysis, we found iPL is more independent on mesh size than HFD. There were insignificant differences in iPL by using 0.5–1.5 mm mesh sizes. In addition, there were insignificant differences by using different numerical solvers for both iPL and HFD. Therefore, if a study only focuses on iPL, the 1 mm mesh size with the SIMPLE steady solver can be a good starting selection for CFD simulation because of (1) the small standard deviation (1.42%) of the percentage difference of iPL by comparing with the results from the 0.5 mm mesh size, and (2) the fastest computation speed of the SIMPLE steady solver.

Different from iPL, there is a significant difference in HFD between the mesh sizes above 1 mm and below 0.7 mm. We found that the HFD results computed with 1 mm match significantly closer to the experimental results than those computed with 0.7 mm. The Fontan models with the 0.7 mm mesh size have denser massless particles uniformly distributed at the inlet boundary surfaces than those with the 1 mm mesh. In
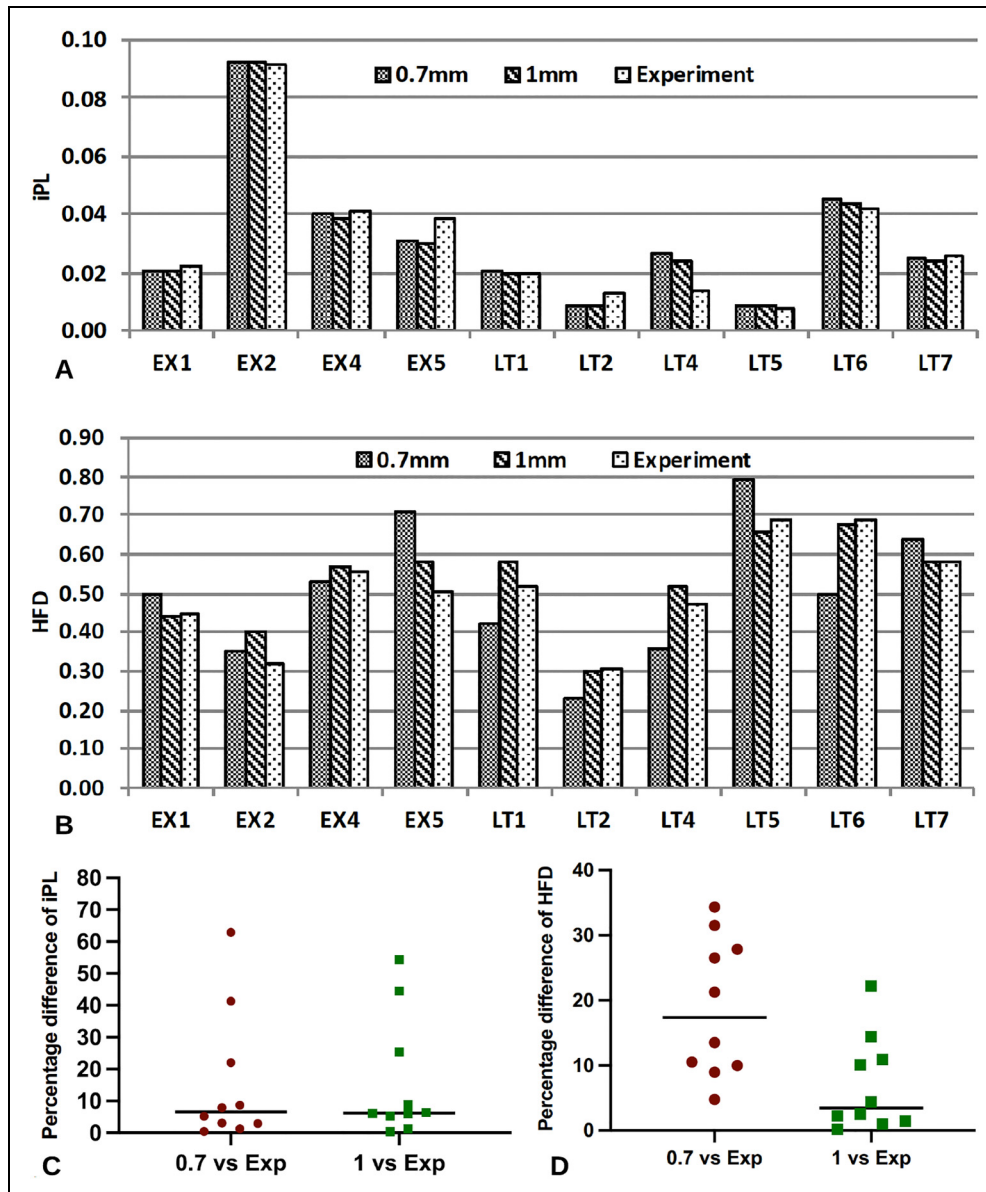
Figure 4. Comparison of iPL and HFD between CFD and experimental results. The CFD results were computed by using 0.7 and 1 mm mesh sizes separately with the SIMPLE-Steady solver.
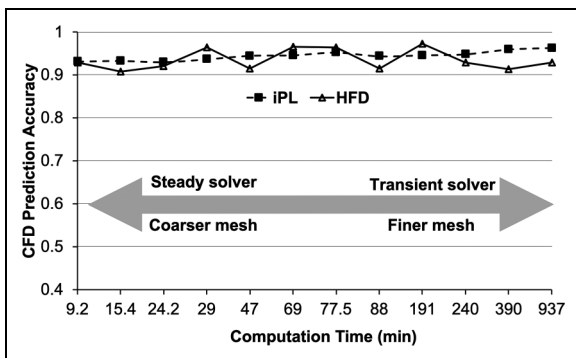Abbreviations: iPL, indexed power loss; HFD, hepatic flow distribution; CFD, computational fluid dynamics.

Figure 5. Computation time and computational fluid dynamics (CFD) prediction accuracy by using different solvers and various mesh sizes to complete the simulations with 3000 iterations on EX5.

our *in vitro* experiment, we used microparticles with the size of 0.85–1 mm. The distribution of the microparticles released at IVC in the experiment matches closer to the simulated particle distribution with the 1 mm mesh in the simulation than that with the 0.7 mm mesh size.

Based on our results, the cumulative probability distributions of the percentage difference between the CFD predicted values and the experimental benchmark values for iPL and HFD are generated (Supplemental material Figure S9). For a CFD simulation of a patient-specific Fontan model, the probabilities of keeping the percentage differences of iPL and HFD below 10% are about 0.6 and 0.8, respectively. Our analysis indicates that the flow competition of IVC and SVC can lead to a significant power loss, which agrees with the finding in a prior study.[32]
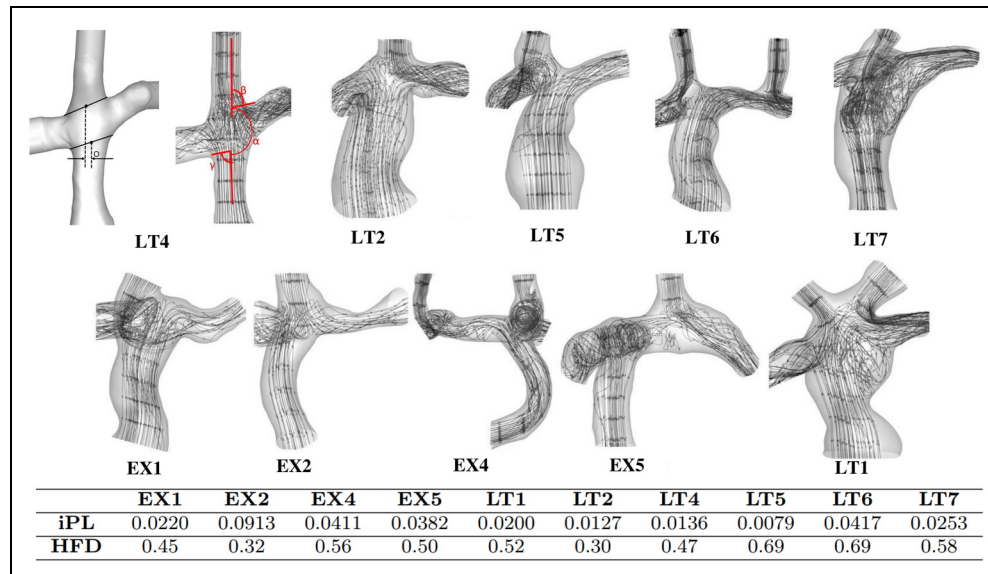
	EX1	EX2	EX4	EX5	LT1	LT2	LT4	LT5	LT6	LT7
iPL	0.0220	0.0913	0.0411	0.0382	0.0200	0.0127	0.0136	0.0079	0.0417	0.0253
HFD	0.45	0.32	0.56	0.50	0.52	0.30	0.47	0.69	0.69	0.58

Figure 6. Analysis of Fontan model geometry and flow streamlines. The offset (O) measured between the center of IVC and SVC where the flows enter the PA, angle between the IVC and SVC flow where they enter the PA. The table at the bottom shows the angle and offset between the flows from IVC and SVC.
Abbreviations: SVC, superior vena cava; IVC, inferior vena cava; PA, pulmonary arteries.

The computational modeling with different solvers used in this study seems insufficient to accurately compute the power loss under this scenario. To predict iPL accurately for these complex models, further computational analysis is needed.

While robust and novel, our work was limited by the limited size variety of the microparticles to fully confirm the influence of mesh size on HFD, as they are not readily commercially available. In addition, we acknowledge that a larger scale of validation is still needed to generate more robust statistics on the accuracy of CFD prediction for cardiovascular surgical planning, which include, but not limited to Fontan surgery. Surgical implantations of planned vascular grafts were executed by using a paper printed ruler as guidance to match the prescribed anastomosis location.[13] More work is required to quantitatively analyze and improve the implantation accuracy. To robustly acquire the flow measurements, during the experiment, we oriented the 3D printed Fontan models in different poses to mimic different orthostatic positions and adjusted the fluid density and viscosity by changing the percentages of water–glycerol mixture from 60/40 to 80/20. Our results show that the measurement changes of iPL and HFD are small enough to ignore. The Nylon polymer used in the 3D printed Fontan model is more rigid than the actual Gore-Tex graft that can resist dilation. Rigid wall assumption is appropriate to be used in Fontan analysis. Prior fluid–structure interaction study showed minimal differences in HFD by comparing rigid and compliant vessel wall simulations.[33] To avoid geometric confliction of Fontan conduit and heart, at the phase of surgical planning, the heart model was used to define the spatial constraint. Further clinical study is needed to confirm how graft–heart interaction affects Fontan hemodynamics. Beyond the scope of this work, effects of noncompliant vessel/chamber walls, respiratory flow changes, flow changes with exercise and the patient's growth, anatomical changes with the patient's growth will be investigated in future study.

Conclusions

Our results show that there are 0.6 to 0.7 probability chances for the CFD simulation to predict the iPL and HFD with higher than 90% accuracy, which indicates that CFD simulation can provide meaningful hemodynamic prediction for Fontan surgical planning. The prediction accuracy can be significantly affected by the model shape complexity and flow competition.

Declaration of Conflicting Interests

The authors declared no potential conflicts of interest with respect to the research, authorship, and/or publication of this article.

Supplemental Material

Supplemental material for this article is available online.

References

1. Shah MJ, Rychik J, Fogel MA, Murphy JD, Jacobs ML. Pulmonary AV malformations after superior cavopulmonary connection: resolution after inclusion of hepatic veins in the pulmonary circulation. *Ann Thorac Surg*. 1997 Apr;63(4):960-963.

2. Shinohara T, Yokoyama T. Pulmonary arteriovenous malformation in patients with total cavopulmonary shunt: what role does lack of hepatic venous blood flow to the lungs play? *Pediatr Cardiol*. 2001 Aug;22(4):343-346.

3. Trusty PM, Slesnick T, Wei ZA, et al. Fontan surgical planning: previous accomplishments, current challenges, and future directions. *J Cardiovasc Transl Res*. 2018;11(2):133-144.

4. McElhinney DB, Marshall AC, Lang P, Lock JE, Mayer JE. Creation of a brachial arteriovenous fistula for treatment of pulmonary arteriovenous malformations after cavopulmonary anastomosis. *Ann Thorac Surg*. 2005 Nov;80(5):1604-1609.

5. Vettukattil JJ. Pathogenesis of pulmonary arteriovenous malformations: role of hepatopulmonary interactions. *Heart*. 2002 Dec;88(6):561-563.

6. Trusty PM, Wei ZA, Slesnick TC, et al. The first cohort of prospective fontan surgical planning patients with follow-up data: how accurate is surgical planning? *J Thorac Cardiovasc Surg*. 2019 Mar;157(3):1146-1155.

7. Khiabani RH, Whitehead KK, Han D, et al. Exercise capacity in single-ventricle patients after fontan correlates with haemodynamic energy loss in TCPC. *Heart*. 2015;101(2):139-143.

8. Loke Y-H, Kim B, Mass P, et al. Role of surgeon intuition and computer-aided design in fontan optimization: a computational fluid dynamics simulation study. *J Thorac Cardiovasc Surg*. 2020;160(1):203-212.e2.

9. Siallagan D, Loke YH, Olivieri L, et al. Virtual surgical planning, flow simulation, and 3-dimensional electrospinning of patient-specific grafts to optimize fontan hemodynamics. *J Thorac Cardiovasc Surg*. 2018;155(4):1734-1742.

10. Liu X, Kim B, Loke Y-H, et al. Semi-Automatic planning and three-dimensional electrospinning of patient-specific grafts for fontan surgery, in *IEEE Trans Biomed Eng*. 2022;69(1):186-198. doi: 10.1109/TBME.2021.3091113.

11. Liu X, Aslan S, Hess R, et al. Automatic shape optimization of patient-specific tissue engineered vascular grafts for aortic coarctation. In: *2020 42nd Annual International Conference of the IEEE Engineering in Medicine & Biology Society (EMBC)*, 2020, pp. 2319-2323, doi: 10.1109/EMBC44109.2020.9176371.

12. Haggerty CM, de Zélicourt DA, Restrepo M, et al. Comparing pre- and post-operative fontan hemodynamic simulations: implications for the reliability of surgical planning. *Ann Biomed Eng*. 2012 Dec;40(12):2639-2651.

13. Yeung E, Inoue T, Matsushita, et al. In vivo implantation of 3-dimensional printed customized branched tissue engineered vascular graft in a porcine model. *J Thorac Cardiovasc Surg*. 2020 May;159(5):1971-1981.e1.

14. Medero R, Ruedinger K, Rutkowski D, Johnson K, Roldán-Alzate A. In vitro assessment of flow variability in an intracranial aneurysm model using 4D flow MRI and tomographic PIV. *Ann Biomed Eng*. 2020 Oct;48(10):2484-2493.

15. Medero R, Hoffman C, Roldán-Alzate A. Comparison of 4D flow MRI and particle image velocimetry using an In vitro carotid bifurcation model. *Ann Biomed Eng*. 2018 Dec;46(12):2112-2122.

16. Roldán-Alzate A, García-Rodríguez S, Rivera L, Wieben O, Anagnostopoulos PV, Francois CJ. Hemodynamic study of TCPC using in vivo and in vitro 4D flow MRI and numerical simulation. *J Cardiovasc Magn Reson*. 2014 Jan;16(S1):W39.

17. Bächler P, Valverde I, Pinochet N, et al. Caval blood flow distribution in patients with fontan circulation: quantification by using particle traces from 4D flow MR imaging. *Radiology*. 2013 Apr;267(1):67-75.

18. Yang W, Chan FP, Reddy VM, Marsden AL, Feinstein JA. Flow simulations and validation for the first cohort of patients undergoing the Y-graft fontan procedure. *J Thorac Cardiovasc Surg*. 2015 Jan;149(1):247-255.

19. Biglino G, Cosentino D, Steeden JA, et al. Using 4D cardiovascular magnetic resonance imaging to validate computational fluid dynamics: a case study. *Front Pediatr*. 2015 Dec 14;3:107. doi: 10.3389/fped.2015.00107. eCollection 2015.

20. Cibis M, Jarvis K, Markl M, et al. The effect of resolution on viscous dissipation measured with 4D flow MRI in patients with fontan circulation: evaluation using computational fluid dynamics. *J Biomech*. 2015 Sep;48(12):2984-2989.

21. DeGroff CG. Modeling the fontan circulation: where we are and where we need to go. *Pediatr Cardiol*. 2008 Jan;29(1):3-12.

22. Haggerty CM, Restrepo M, Tang E, et al. Fontan hemodynamics from 100 patient-specific cardiac magnetic resonance studies: a computational fluid dynamics analysis. *J Thorac Cardiovasc Surg*. 2014;148(4):1481-1489.

23. A-to-Z Guide to Thermodynamics, Heat and Mass Transfer, and Fluids Engineering: AtoZ. Vol. E. Begellhouse; 2006.

24. Glycerin Producer's Association (author). Physical properties of glycerine and its solutions. Glycerine Producers' Association. New York, 1963.

25. Kenner T. The measurement of blood density and its meaning. *Basic Res Cardiol*. 1989 Apr;84(2):111-124.

26. Baskurt OK, Meiselman HJ. Blood rheology and hemodynamics. *Semin Thromb Hemost*. 2003 Oct;29(5):435-450.

27. Wei ZA, Huddleston C, Trusty PM, et al. Analysis of inlet velocity profiles in numerical assessment of fontan hemodynamics. *Ann Biomed Eng*. 2019 Nov;47(11):2258-2270.

28. Fogel MA, Pawlowski TW, Whitehead KK, et al. Cardiac magnetic resonance and the need for routine cardiac catheterization in single ventricle patients prior to fontan: a comparison of 3 groups: pre-fontan CMR versus cath evaluation. *J Am Coll Cardiol*. 2012 Sep 18;60(12):1094-1102.

29. Akintoye E, Miranda WR, Veldtman GR, Connolly HM, Egbe AC. National trends in fontan operation and in-hospital outcomes in the USA. *Heart Br Card Soc*. 2019 May;105(9):708-714.

30. Fogel MA, Trusty PM, Nicolson S, et al. Cross-Sectional magnetic resonance and modeling comparison From just after fontan to the teen years. *Ann Thorac Surg*. 2020 Feb;109(2):574-582.

31. Srivastava D, Preminger T, Lock JE, et al. Hepatic venous blood and the development of pulmonary arteriovenous malformations in congenital heart disease. *Circulation*. 1995 Sep 1;92(5):1217-1222.

32. de Leval MR, Dubini G, Migliavacca F, et al. Use of computational fluid dynamics in the design of surgical procedures: application to the study of competitive flows in cavopulmonary connections. *J Thorac Cardiovasc Surg*. 1996 Mar 1;111(3):502-513.

33. Long CC, Hsu M-C, Bazilevs Y, Feinstein JA, Marsden AL. Fluid-structure interaction simulations of the fontan procedure using variable wall properties. *Int J Numer Methods Biomed Eng*. 2012;28(5):513-527.